Environmental Pollution 300 (2022) 118939

Contents lists available at ScienceDirect

Environmental Pollution

journal homepage: www.elsevier.com/locate/envpol

Periodate activated by manganese oxide/biochar composites for antibiotic degradation in aqueous system: Combined effects of active manganese species and biochar☆

Guoge Fang[a,b,1], Jialing Li[c,1], Chen Zhang[a,b,*], Fanzhi Qin[a,b], Hanzhuo Luo[a,b], Cheng Huang[a,b], Deyu Qin[a,b], Zenglin Ouyang[a,b]

[a] *College of Environmental Science and Engineering, Hunan University, Changsha, 410082, PR China*
[b] *Key Laboratory of Environmental Biology and Pollution Control, Ministry of Education, Hunan University, Changsha, 410082, PR China*
[c] *School of Design, Hunan University, Changsha, Hunan, 410082, PR China*

ARTICLE INFO

Keywords:
Modified biochar
Active manganese species
Periodate
Advanced oxidation processes (AOPs)
OTC degradation

ABSTRACT

Developing efficient catalysts for oxytetracycline (OTC) degradation is an ideal strategy to tackle environmental pollution, and advanced oxidation processes (AOPs) have been widely used for its degradation. However, the studies on the activation of periodate (PI) by biochar and its composites in recent years have been scarcely reported. In this study, we focused on the degradation of OTC by PI activation with manganese oxide/biochar composites (Mn_xO_y@BC). Experimental results showed that the OTC degradation rate of Mn_xO_y@BC/PI system reached almost 98%, and the TOC removal efficiency reached 75%. Various characteristic analysis proved that PI could be activated efficiently by surface functional groups and manganese-active species (Mn(II), Mn(III), and Mn(IV)) on biochar, and various reactive species such as singlet oxygen ($^1O_2$), hydroxyl radical (•OH), and superoxide radical ($O_2^{\bullet-}$) can be observed via radical quenching experiments. Based on this, three degradation pathways were proposed. Furthermore, Mn_xO_y@BC and PI were combined to degrade environmental pollutants, which achieved excellent practical benefits and had great practical application potential. We hope that it can provide new ideas for advanced oxidation processes (AOPs) applying for wastewater treatment in the future.

1. Introduction

With increasing population and factories, antibiotics are becoming an important class of pollutants in the aquatic environment. Oxytetracycline (OTC), as a broad-spectrum antibiotic, can effectively prevent diseases with low cost. However, it will bring about eco-toxicological risk when released to water bodies (Zhang et al., 2021a). Therefore, it is meaningful to find an effective and eco-friendly method to remove OTC from water matrix (Huang et al., 2017a; Yang et al., 2020b). Recently, advanced oxidation processes (AOPs) have been widely used for antibiotic degradation in water bodies (Yang et al., 2020a). Normally, the oxidants used in AOPs include hydrogen peroxide (H_2O_2), persulfate (PS), and ozone, which can successfully combine with active catalysts and trigger reactive oxygen species (ROS) evolution (Song et al., 2022; Yang et al., 2019). Liu et al. studied that combing magnetic nitrogen doped biochar with PS can efficiently generate sulfate radical for metolachlor degradation (Liu et al., 2020). Zhang et al. found that permanganate/visible light (PM/VL) system has excellent performance on sulfamethazine degradation, and a catalyst-free pollutants degradation system was proposed (Zhang et al., 2021b). Although the PM/VL system can effectively degrade pollutants, its activation efficiency needs to be further improved. Compared with other oxidants, periodate (PI) is a novel oxidants with advantages of more versatile and stable, strong oxidation, and convenient transportation (Zong et al., 2021). For AOPs dominated by PI, the active intermediates including $\bullet IO_3$ and reactive oxygen species (ROS, e.g., $O_2^{\bullet-}$, •OH, and $^1O_2$) were generally formed through electronic transfer and can effectively degrade organic pollutants (Yun et al., 2017). Nowadays, ultraviolet rays (UV) or visible light radiation (VL), alkali, transition metals, and ultrasound have been developed for activing catalysts and degrading pollutants (Cao et al.,

---

☆ This paper has been recommended for acceptance by Jörg Rinklebe.

* Corresponding author. College of Environmental Science and Engineering, Hunan University, Changsha, 410082, PR China.
E-mail address: zhangchen@hnu.edu.cn (C. Zhang).

[1] These authors contribute equally to this article.

https://doi.org/10.1016/j.envpol.2022.118939
Received 6 October 2021; Received in revised form 25 January 2022; Accepted 30 January 2022

2010; Chia et al., 2004; Lee et al., 2016; Sun et al., 2020). But the main deficiencies of these methods are large-equipment consumption and the high-cost, it is necessary to find cheap, efficient, and green activators, which is essential for PI-based wastewater treatment (Tan et al., 2021).

Biochar is a carbon-rich solid product obtained by a high-temperature pyrolysis of forestry, industrial organic, and agricultural waste under anoxic conditions (Qin et al., 2021; Zhang et al., 2019a; Zhang et al., 2019b). It has received a lot concern of researchers due to its high specific surface, multiple functional groups, and excellent resistance for acid and alkali corrosion (Huang et al., 2017b). Firstly, biochar is a widely used adsorbent due to its pore filling effect, π-π stacking interaction, hydrogen bonding, and low cost (Xiang et al., 2020; Zhang et al., 2016). So far, researchers have found that it can absorb heavy metals in water and soil, such as cadmium (Cd) (Xu et al., 2017), copper (Cu) (Peng et al., 2017), arsenic (As) (Cuong et al., 2021), plumbum (Pd) (Wang et al., 2021), and et al. (Melia et al., 2019). In the process of adsorption, many reaction principles are involved, including redox reaction, chemical precipitation, and surface complexation. Moreover, researchers have investigated that biochar can be an ideal photo-catalyst. Ye, Meng, and Fang et al. had all studied the photocatalytic capacity of biochar (Fang et al., 2017; Meng et al., 2020; Ye et al., 2019). Moreover, biochar is also used as mediator for AOPs, and persistent free radical (PFRs) and •OH can be produced due to the large number of functional groups on its surface, which can degrade organic pollutants (Kumar et al., 2020). However, it is insufficient for pristine biochar to remove pollutants due to its limited adsorption and degradation capacity. Therefore, modification for improving its performances to achieve the desired removal efficacy is urgently needed (Liu et al., 2020).

There were many reports for the modification of biochar, especially transition metals (Trakal et al., 2016; Zhang et al., 2021c). Recently, Nano-scale Fe^0 have been studied extensively for producing ROS in removing antibiotics (Li et al., 2020; Zhao et al., 2020). Other recent literatures have reported that researchers have tried to enhance the biochar effectiveness by modified with $MnFe_2O_4$ (Lin et al., 2021), MgO (Shen et al., 2019), CuO/Cu (Xu et al., 2018), and so on. Manganese, as a kind of transition metal, is widely distributed in nature with low cost and promising performances compared with other metals. It has been extensively used to modify biochar for catalytic degradation of organic pollutants. The degradation mechanism of organic pollutants by manganese/manganese oxides-mediated PI oxidation systems has been well studied (Du et al., 2019; Du et al., 2020). It can be concluded that using manganese as PI activator can effectively produce free radicals and degrade pollutants. However, pure Mn^{2+} have ecological risk in the natural environment. Besides, the overall effective catalytic capacity of pure Mn oxides was reduced by agglomeration. Therefore, we combined biochar with manganese oxides to mediate PI for OTC degradation. Biochar composites possessed two advantages, one is the stable oxide making Mn ions at a lower level in aquatic environment, the other is that it can also effectively disperse particles of Mn (Wang et al., 2018). Moreover, the cost of this system could be reduced via using agricultural waste as biochar feedstock. However, to the best of our knowledge, the studies on the activation of PI by manganese oxide modified biochar in recent years have not been reported.

Therefore, in this work, the corn straw was used as biochar feedstock, and manganese oxide modified biochar (Mn_xO_y@BC) was synthesized by simple impregnation and high temperature pyrolysis. Various characterizations for materials were conducted and the removal performances of representative organic contaminants in the Mn_xO_y@BC/PI process were evaluated. The degradation pathways with intermediates and degradation products were explored with HPLC-MS analysis. More importantly, the activation mechanism was studied and the possibility of practical application was proposed.

2. Materials and methods

2.1. Materials and reagents

OTC was obtained from Sinopharm Chemical Reagent Co., Ltd., and its physicochemical properties were listed in Table S1. Manganese chloride tetrahydrate ($MnCl_4$•$4H_2O$), potassium periodate (KIO_4, 99%), manganese oxide (MnO), manganese dioxide (MnO_2), hydrochloric acid (HCl), sodium hydroxide (NaOH), phosphoric acid (PA), and sodium thiosulfate ($Na_2S_2O_8$) were also obtained from Sinopharm Chemical Reagent Co., Ltd. The solutions used in the experiments were all configured with deionized water (18.25 MΩ cm) and except corn straw, all the other chemicals were at least analytically pure and no further purification is required.

2.2. Preparation of activators

The Mn_xO_y@BC was prepared in the following way: corn straw was washed with deionized water, dried overnight at 80 °C, and passed through a 100-mesh sieve (Yang et al., 2021b). After sieving, 10 g of the feedstock was immersed in 100 mL 10 g/L $MnCl_4$•$4H_2O$ solution and ultrasonically vibrated for 30 min, steeped at 80 °C for 2 h, and then dried overnight at 60 °C. The resulting precursors were charred at 500 °C for 2 h at a heating rate of 5 °C/min under nitrogen (N_2) atmosphere (Tan et al., 2020). The Mn_xO_y@BC was washed and ground, passed through 100-mesh sieve for later experiments, named MBC. The same process was used for pristine biochar, named BC.

2.3. Characterization and analytical methods

Brunauer-Emmett-Teller (BET) was measured on a Micromeritics ASAP 2020 HD88 instrument, which could obtain the surface area and pore distribution of BC and Mn_xO_y@BC. The morphology of samples was measured by Zeiss Sigma 300 scanning electron microscopy (SEM). The microstructure and elemental distribution of materials were recorded by FEI Tecnai G2 F20 S-TWIN Transmission electron microscopy (TEM) and energy disperses X-ray spectroscopy (EDS) mapping profiles. The X-ray diffraction (XRD) was examined on a Bruker AXS D8 Advances. A Horiba Jobin Yvon LabRAM HR800 Raman and a Thermo Nicolet 5700 spectrophotometer were used to investigate the Raman spectrum and the Fourier transform infrared spectrometer (FT-IR), respectively. CHI760E electrochemical workstation was used in this research to analyze the electrochemical impedance spectroscopy (EIS) of samples. In addition, X-ray photoelectron spectroscopy (XPS) was used to analyze the structure and properties of materials on a Thermo Escalab 250Xi spectrometer. Electron spin resonance (ESR) was also conducted on a Bruker ER200-SR, using 5,5-dimethyl-1-pyrroline N-oxide (DMPO) and 2,2,6,6-tetramethylpiperidine (TEMP) as trapping agents to identify radicals. Total organic carbon (TOC) was measured to demonstrate the mineralization of OTC by Shimadzu TOC-L analyzer. The intermediate of OTC degradation was measured by high-performance liquid chromatography-triple quaternary rod tandem mass spectrometer (HPLC-MS, Agilent).

2.4. Catalytic degradation experiments

All experiments were conducted under magnetic agitation (420 r/min). Typically, 0.25 mM of PI was added into the solution and the concentration of OTC was 20 mg/L. Next, at preset response intervals (0, 2, 4, 6, 8, 10, 15, 20, 30 min), 1 mL was sampled and filtered with a 0.22 μm filter. It was immediately mixed with 100 μL $Na_2S_2O_8$ to terminate the reaction, and added into a chromatography sample bottle for the next analysis. Finally, the high-performance liquid chromatograph (HPLC) was employed to analyze the OTC concentration. To ensure reproducibility, all experiments were done at least three times.

3. Results and discussion

3.1. *Characterization of materials*

The morphologies of the BC and Mn_xO_y@BC materials are determined by SEM and TEM. As shown in Fig. 1(a–d), it can be obtained that the pristine biochar had a smooth surface and existed in the form of flakes while the modified biochar had a lot of spherical particles attached on the surface uniformly. In addition, the shadow distribution performed by TEM image in Fig. 1i proved the particles loaded again. The images of EDS elemental mapping (Fig. 1e–h) showed that Mn elements are uniformly distributed. Moreover, the BET surface areas of BC and Mn_xO_y@BC (Table S2) are 79.46 and 238.97 m^2/g, and the pore size of them decreased from 10.13 nm to 2.06 nm. The reason of the increasing surface area might be the loading of Mn oxide. It can be concluded that Mn oxide was loaded on the surface of biochar successfully, indicating the successful preparation of the proposed composites.

The structures of BC and Mn_xO_y@BC samples were confirmed by XRD analysis (Fig. S1). XRD patterns of BC had broad peaks with 2θ at around 23° and around 40°, which were attributed to the amorphous structure of graphite of biochar. While the peaks at 26.4° in BC, which represent (002) of crystal planes of graphite (JCPDS NO. 26-1079) (Stephan et al., 2006). Compared to BC, there was no obvious change of XRD spectrum in Mn_xO_y@BC, which may be caused by the little-doping of manganese species during the synthesis process. To further studying the surveys and the bonding types of BC and Mn_xO_y@BC, the tests of XPS were conducted. As were shown in Fig. 2. The peaks at around 284.7 eV, 400.0 eV, 533.2 eV, and 642.2 eV are shown in the XPS survey spectrum of BC and Mn_xO_y@BC samples, which corresponds to C, O, N, and Mn as the center of the bond, respectively (Luo et al., 2019). It can be seen from Fig. 2a that in the surveys of BC and Mn_xO_y@BC, C, N, and O can be seen obviously. However, a new peak of Mn element was generated in the survey of Mn_xO_y@BC, which means that the Mn is successfully loaded to the surface of Mn_xO_y@BC. In Fig. 2b, the peaks of C1s in BC at 284.5, 285.6, 288.6, and 289.6 eV correspond to C–C, C–O, C=O and π-π* shake up, respectively. While in Mn_xO_y@BC, the C1s spectra had O=C–O bonds at 286.9 eV (Qin et al., 2020). The O1s of BC could be fitted into 531.9, 532.3, and 533.1 eV,

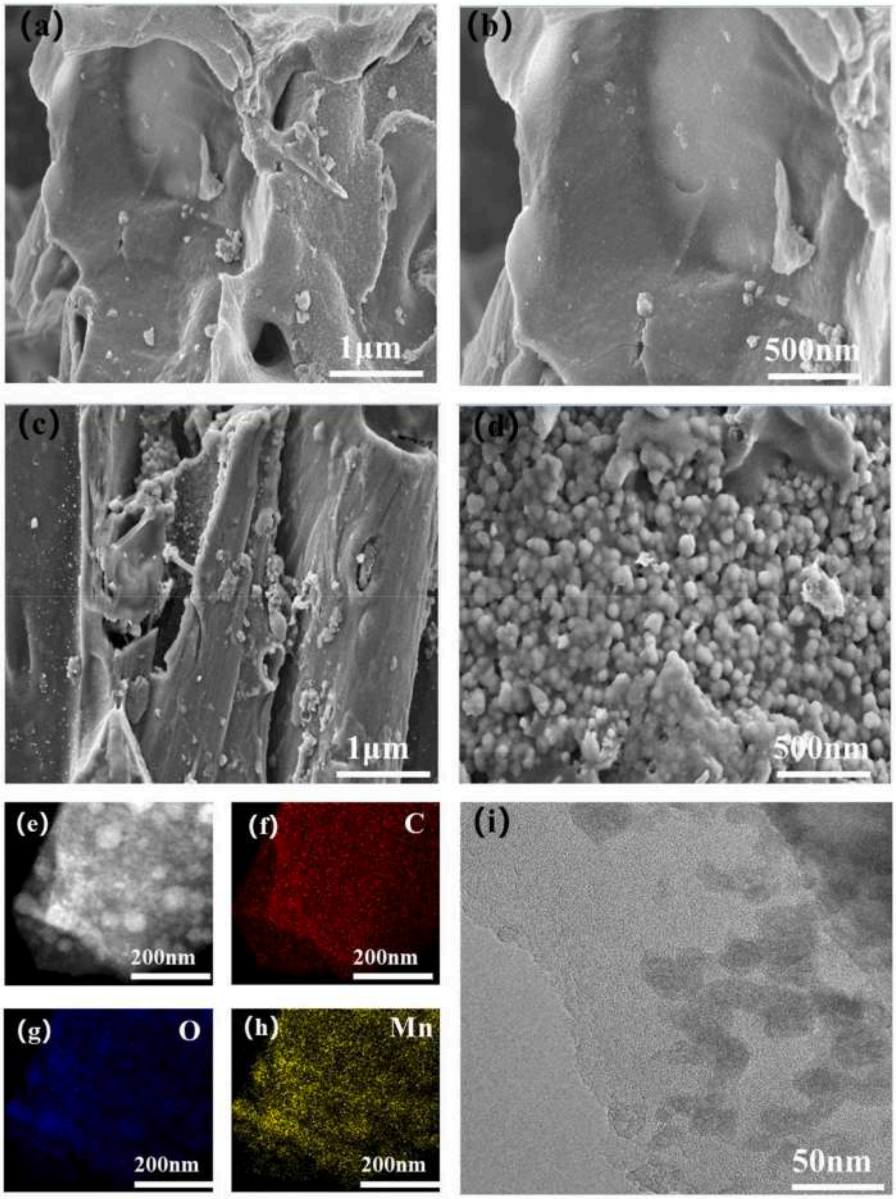

Fig. 1. SEM images of BC (a, b) and Mn_xO_y@BC (c, d); EDS elemental mapping images of Mn_xO_y@BC (e–h); TEM images of Mn_xO_y@BC (i).

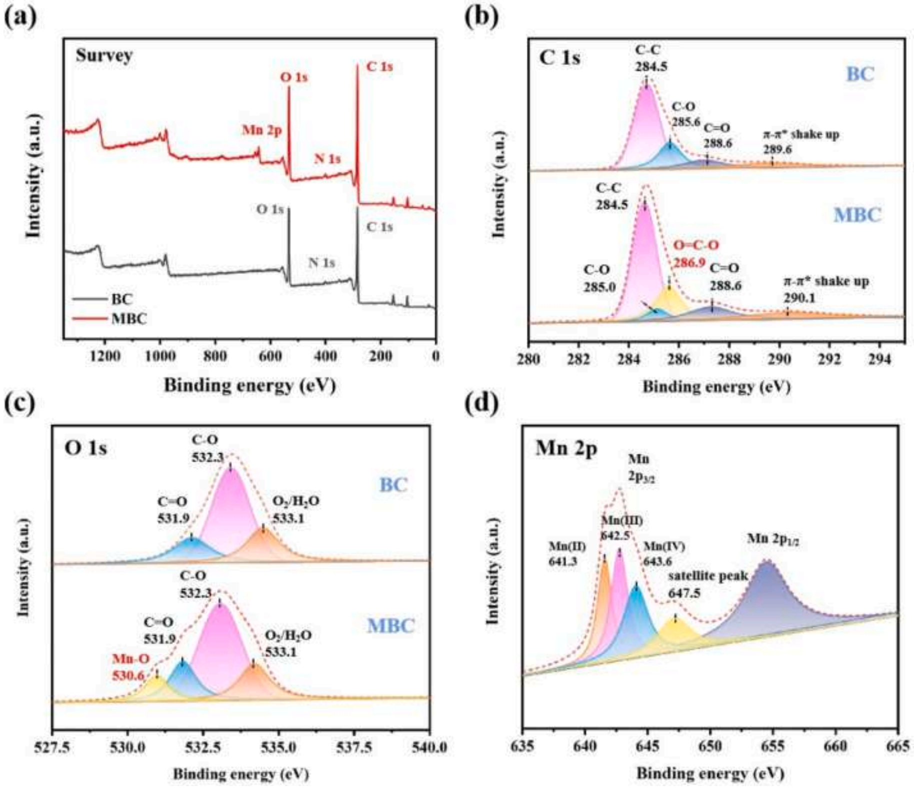

Fig. 2. XPS spectra for BC and Mn_xO_y@BC: a) survey spectra, b) C1s, c) O1s, and d) Mn2p.

which representing the vibration of O_2/H_2O, C–O, and C═O, respectively (Fig. 2c). A new peak belonging to Mn–O is formed at the 530.6 eV position of the O1s spectrum in Mn_xO_y@BC. Compared to the BC, the C═O in the composite was significantly increased, and the amount of C–O showed decreasing trend, it can be concluded that the surface functional groups of samples have transformed after modification, which was better to enhance the removal efficiency of OTC (Qin et al., 2020; Zhou et al., 2011). XPS spectrum of Mn2p was shown in Fig. 2d, it can be received that it was composed of a spin-orbit doublet of $Mn2p_{1/2}$ and $Mn2p_{3/2}$. The three peaks of $Mn2p_{1/2}$ at 641.3, 642.5, and 643.6 eV corresponded to Mn(II), Mn(III), and Mn(Ⅳ), respectively. Moreover, XPS Spectra of $Mn2p_{3/2}$ in all samples showed the satellite feature at 647.5 eV. These polyvalent manganese species are an important reason for the high catalytic activity of the materials (Jia et al., 2020; Wan et al., 2016; Yang et al., 2021b). The existence form of active manganese species in this reaction system can also be known.

The degree of defects and graphitization of BC and Mn_xO_y@BC were analyzed by Raman spectroscopy. As shown in Fig. S2a, the D band between 1340 and 1360 cm^{-1} and the G band between 1580 and 1600 represented disordered carbon or defective carbon and ordered carbon or the existence of sp^2 hybridization, respectively, and the value of I_D/I_G was usually used to reflect the degrees of graphitization (Chen et al., 2020). The I_D/I_G value of Mn_xO_y@BC was 0.672, which was higher than the value of BC (0.663). This result reflected that Mn_xO_y@BC has more defects because of the loading of Mn which is also the reason of the higher catalytic activity. The FTIR analysis of samples was shown in Fig. S2b. The peak at 2922 cm^{-1} of BC was attributed to the C–H, which was decreased with the Mn loading in Mn_xO_y@BC. In addition, the peaks at 881, 1070, and 1580 cm^{-1} were attributed to the stretching vibration of C–C, C–O, and C═O, respectively (Yan et al., 2018). While compared with BC, the peak at 3380 cm^{-1} of Mn_xO_y@BC was ascribed to the vibrations of Mn–O bond, which further verified the results of XPS analysis (Ishii et al., 1972).

The electrochemical properties of samples were evaluated by the EIS analysis. It can be seen from Fig. S3 that the semicircle diameter of Mn_xO_y@BC is smaller than BC, which indicating that Mn_xO_y@BC has a lower electron transfer resistance and is meaningful for efficient charge separation and transform during the reaction (Guo et al., 2019).

3.2. *Catalytic performance of Mn_xO_y@BC*

In order to remove OTC from water bodies and discuss the whole effect of BC and Mn_xO_y@BC materials for its degradation, batch experiments were carried out. As shown in Fig. 3a, the doping ratio of materials (the doping ratio refers to the mass ratio of biomass to $MnCl_2{\bullet}4H_2O$) was studied, when it changed from 3:1 to 9:1, the degradation efficiency did not change obviously. In consideration of cost and safety, we determined that the doping ratio of the materials used in the experiment was 9:1. Moreover, the OTC removal effects of various materials were displayed, including MnO, MnO_2, BC, and Mn_xO_y@BC. As shown in Fig. 3a, comparing the removal efficiency of OTC, the Mn_xO_y@BC/PI system showed the best performance of degradation, up to 97.5% in 30 min reaction and was about 50% higher than that of BC. It can be seen notably, the removal rate of Mn_xO_y@BC/PI system was better than others obviously and the latest studies about using carbon-based activators to degrade organic pollution were listed in Table 1. It indicated that the Mn_xO_y@BC has strong activation effect towards PI in the reaction system (Yang et al., 2021b). In addition, the adsorption effects of different samples were showed in Fig. S4. The OTC degradation performance with various materials can be fitted by pseudo-first-order reaction model well. The rate constant (k) of MnO_2, MnO, BC, and Mn_xO_y@BC are proportional to their dosage (Fig. 3b). The effects of dosage of Mn_xO_y@BC and PI in degrading OTC were also presented in Fig. S5. As revealed, with the increase of Mn_xO_y@BC dosage from 0.1 g/L to 0.4 g/L, the reaction rate sharply enhanced. However, considering the factors of economic and environmental efficiency, the best fit Mn_xO_y@BC dosage used in the experiment was 0.3 g/L. In addition, the dosage of PI was also explored in this experiment

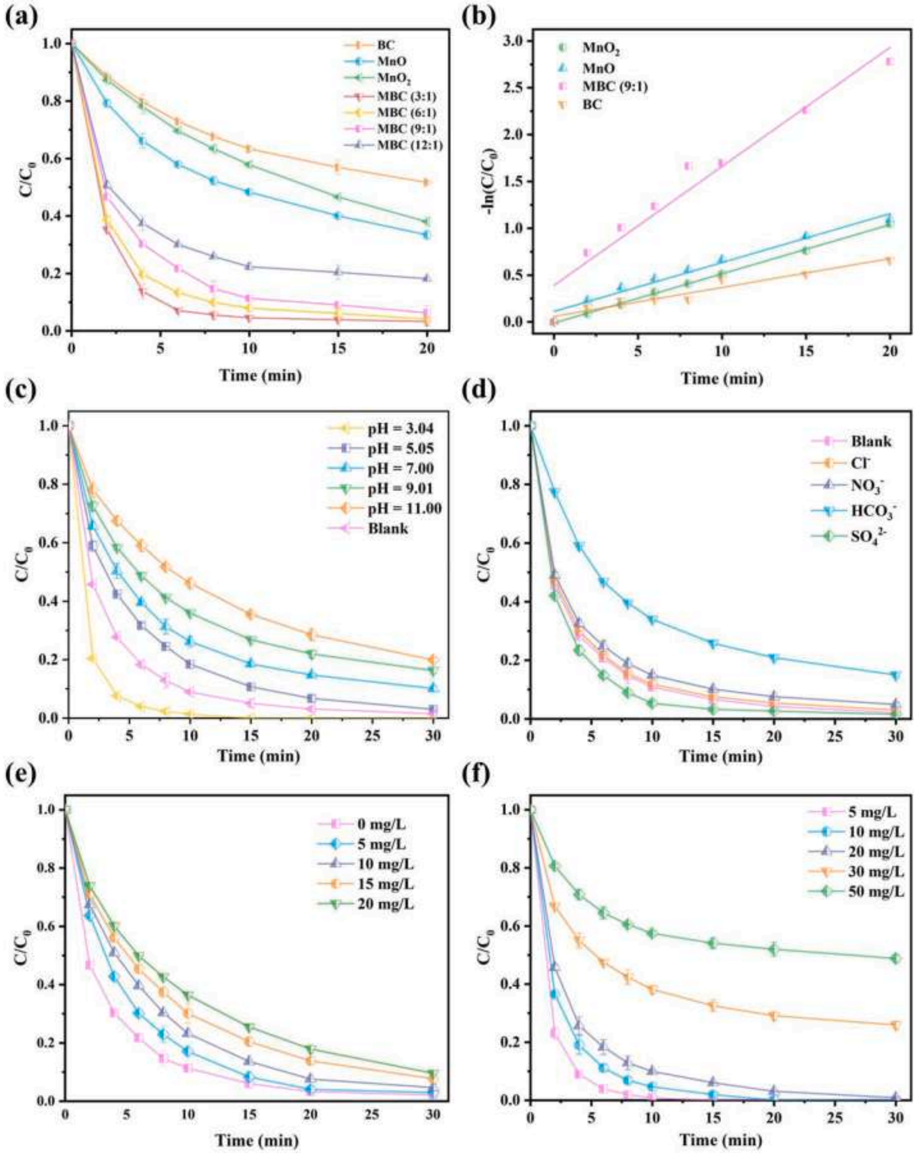

Fig. 3. Removal amount of OTC with different materials (a) and the first-order kinetic fitting results (b) for MnO_2, MnO, BC and Mn_xO_y@BC; Effects of (c) solution pH (3, 5, 7, 9, 11); (d) anions ($[HCO_3^-] = [SO_4^{2-}] = [Cl^-] = [NO_3^-] = 0.5$ mM); (e) HA; (f) OTC concentration. Reaction conditions: PI = 0.25 mM; OTC = 20 mg/L; Mn_xO_y@BC = 0.3 g/L; T = 25 °C.

Table 1
Comparison with other carbon-based activators for organic pollutants degradation.

Activators	Biochar feedstock	Pollutant concentration (mg/L)	Reaction system	Dosage (g/L)	Degradation efficiency	Ref.
FeNiZn-LBC	lignin	OTC (60)	–	0.2	96.1%	Lin et al. (2021)
nMnO_2-BC	bamboo	OTC (100)	–	0.67	96.5%	Feng et al. (2021)
NH_4^+-BC	cassava	OTC (30)	–	–	94%	Luo et al. (2021)
N-BC	straw	TC (20)	–	0.2	90%	Zhong et al. (2021)
ZnO/biochar	roots and stems-leaves	TC (50)	PS	0.1	90.81%	Xu et al. (2022)
Biochar (BBC)	swine bone	ACT (20)	PS	0.1	100%	Zhou et al. (2021)
β-CD modified biochar (β-SB)	sludge	BPA (20)	PDS	0.4	91.6%	Pei et al. (2022)
Fe_2O_3@LBC	loofah	CEX (10)	PS	0.4	73.9%	Song et al. (2021)
GBC	goethite	TC (30)	PMS	0.05	70%	Guo et al. (2021)
This work	cornstalk	OTC (20)	PI	0.3	97.5%	This work

(Fig. S5b). It can be noticed that the degradation rate increased obviously with the dosage adding from 0 mM to 0.25 mM, and it changed slightly after adding above 0.25 mM which might result from the oversupply of PI and the insufficient active sites in Mn_xO_y@BC for reacting (He et al., 2021a). These results concluded that the number of active sites provided by activators played an important role in the oxidation process of OTC activated by PI (Du et al., 2020).

In addition, the solution pH affects the species of PI and pollutants (Du et al., 2020). The pH value was set at 3-11 in experiments, with 5 gradients (Fig. 3c). It can be noted that with the pH reducing from 11 to

3, the removal rate increased, and the best degradation efficiency achieved when pH was 3. The reason could be that i) the main form of manganese in the system was Mn(Ⅳ), it showed more reactive at $pH < 7$ (Xu et al., 2018; Zhang et al., 2021b) and ii) when pH is between 3 and 5, H_3L^+ (L represents OTC) is the dominant form of OTC, which has the highest distribution coefficient. When pH is from 5 to 11, $H_2L^{\pm}$ transformed into HL^-, and L^{2-}, most target pollutant particles are in the neutral and negative state (Jin et al., 2017). Therefore, in the acidic environment, the protonated OTC had basically the same charged properties with the Mn_xO_y@BC surface and can fully contact with the material, showing excellent degradation effect. Besides, the removal effect was still high when pH is neutral, indicating a universal pH range of efficiency.

The effect of anions (e.g., NO_3^-, HCO_3^-, Cl^-, and SO_4^{2-}) and HA on OTC removal was also performed in the experiments. As shown in Fig. 3d, the removal efficiency of OTC was not much influenced in the presence of SO_4^{2-}, Cl^-, and NO_3^-, but slightly inhibited by the presence of HCO_3^-. The effect of Cl^- and NO_3^- can be neglected, which indicated that Mn_xO_y@BC/PI process was resistant to the interferences of these anions. SO_4^{2-} was also theoretically considered as an inert ion and didn't react with free radicals in the process, while it had some effect in promoting the reaction. The cause of the effect may be through controlling the kinetics of generating radicals and minimizing the sharp peak, thereby decreasing the precious radicals wasting, so that can promote the degradation of OTC (Yang et al., 2021a). For the inhibitory effect of HCO_3^-, on the one hand, the addition of HCO_3^- will increase the pH of the solution. On the other hand, HCO_3^- are typical radical scavengers which have a strong influence on radical-dominating reactions (Ma and Graham, 2000), thus leading to a low level of degradation. Fig. 3e showed the influence of HA on the process of OTC removal. The results indicated that the existence of HA showed a negative influence on the degradation of OTC, and this effect was proportional to the concentration of HA, which might be due to that HA adsorbed onto the surface of materials and occupied the active sites of reactive Mn species. The OTC degradation would be competed or interfered by the presence of HA to some extent. Meanwhile, in order to prove the applicability and practicality of the materials, the initial concentration of OTC was set from 10 mg/L to 50 mg/L (Fig. 3f). The results showed that when low concentration of OTC exits in the aqueous system, it can be completely degraded in 30 min. With the initial OTC

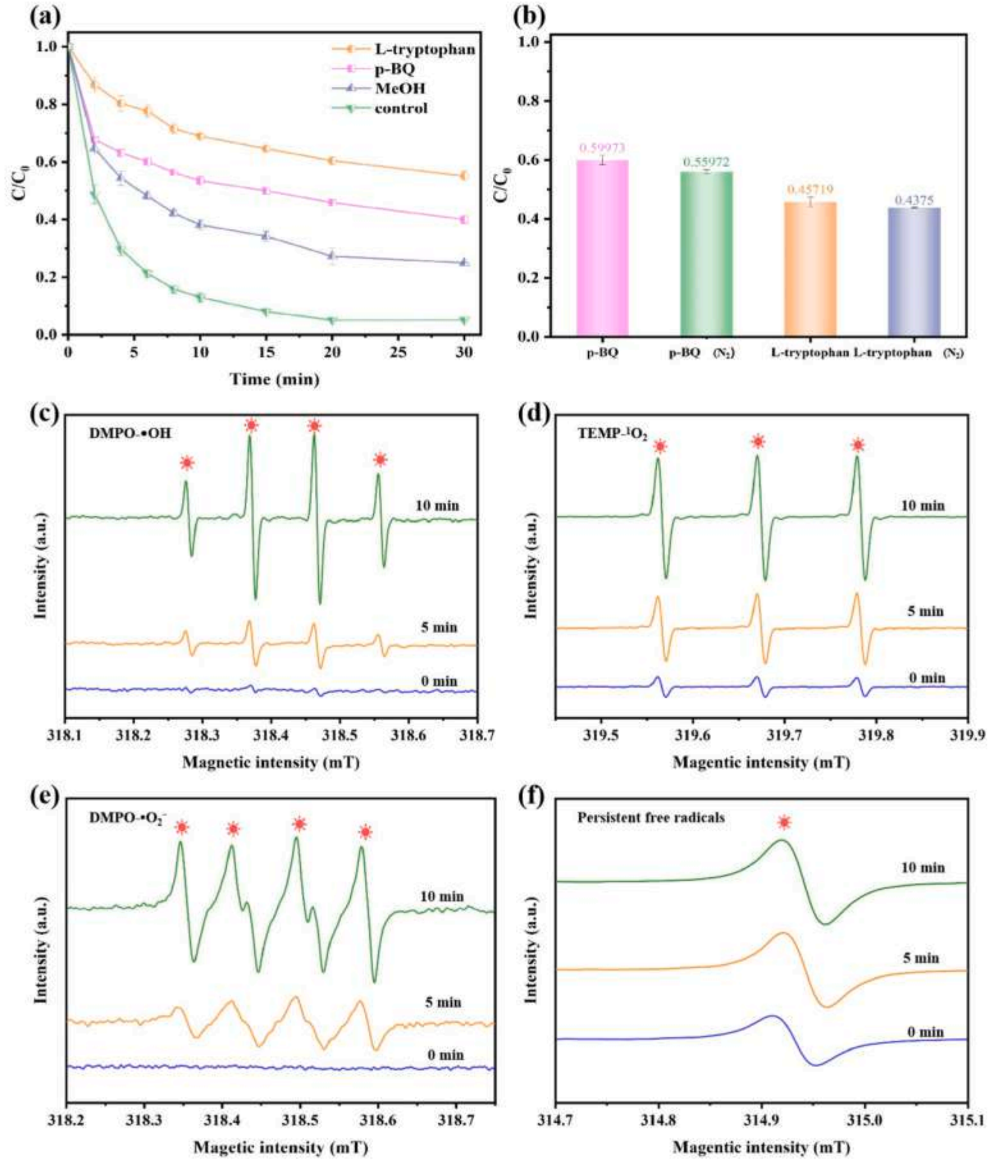

Fig. 4. Identification the influence of non-aeration (a) and aeration (b) treatment on the quenching reaction of reactive species; Identification of dominated reactive species and ESR results of (c) •OH; (d) $^1O_2$; (e) $O_2^{\bullet-}$, and (f) persistent free radicals trapped by DMPO and TEMP at leaching time for 0, 5, and 10 min.

concentration increasing even high as 50 mg/L, more than 50% removal rate was achieved. Studies have shown that the level of OTC in natural water is less than a hundred ng/L, and the prepared materials can still achieve excellent efficiency in a high OTC level, effectiveness and practicality can be concluded (He et al., 2020). Considering the content of OTC in the actual water and feasibility of experimental operation, [OTC] = 20 mg/L was selected.

3.3. Analysis of catalytic mechanism

3.3.1. Main reactive species

In order to explain the mechanism during reaction process and determine kinds of reactive species that dominate the reaction, ESR analysis and quenching experiments were conducted. In quenching experiments, reactive species generated by the BC and Mn_xO_y@BC were quenched by adding Methanol ([MeOH] = 0.25 mM), p-benzoquinone ([PBQ] = 0.25 mM), and L-tryptophan ([L-TRP] = 0.25 mM), which were usually used as the quenching agents for •OH, $^1O_2$, and $O_2^{\bullet -}$, respectively. As shown in Fig. 4a, when L-TRP, PBQ, and MeOH were added to the reaction solution, the OTC degradation rates were reduced from 98% to 60%, 45%, and 85% after 30 min of reaction. To figure out the function of dissolved oxygen for the transform between $^1O_2$ and $O_2^{\bullet -}$, N_2 was introduced into the reaction system to perform anaerobic experiments (Fig. 4b). The results showed that the degradation rate was reduced from 59.97% to 45.71%–55.71% and 43.75%, respectively. The results showed that the conversion between $^1O_2$ and $O_2^{\bullet -}$ is almost negligible. Therefore, $O_2^{\bullet -}$ played the dominant role for the degradation of OTC in Mn_xO_y@BC/PI system, followed by $^1O_2$ and •OH. To further verify the accuracy of the results, ESR analysis with 2,2,6,6-tetramethylpiperidine (TEMP) and 5,5-dimethyl-1-pyrroline N-oxide (DMPO) was conducted. It can be seen in Fig. 4c–e, the characteristic signals of DMPO-•OH, TEMP-$^1O_2$, and DMPO-$O_2^{\bullet -}$ were 1:1:1, 1:1:1:1, and 1:2:2:1, respectively (Zhang et al., 2022). Fig. 4f showed that there was no significant change of the signals. These results were corresponding to the quenching tests. It could be proposed that $O_2^{\bullet -}$ played dominated roles in the reaction with OTC during the degradation process, followed by $^1O_2$ and •OH.

3.3.2. Identification of degradation products and proposed degradation pathways

The possible degradation pathways of OTC were analyzed by HPLC-MS to investigate the intermediate products. The MS spectrum of OTC degradation and intermediates structures were shown in Fig. S6 and Table S3, respectively. Referring to previous literatures and results of HPLC-MS (Yang et al., 2020b; Zhou et al., 2022), the possible degradation pathways were proposed and exhibited in Fig. 5. The possible OTC degradation process mainly includes quinonization, demethylation, dehydration, deamidation, hydroxylation, and ring opening reactions. Firstly, OTC (m/z = 460.9) is transformed to OTC 1 (m/z = 475) through quinonization reaction and hydroxylation reaction. Afterwards, it decomposes to OTC 4 (m/z = 338) via decarboxamidation, deamidation, dihydroxylation, and demethylation pathways. Subsequently, OTC 6 (m/z = 302) is formed through the ring opening. Then, OTC 6 is transformed to OTC 8 (m/z = 226) via decarboxylation and dehydroxylation pathways. Further, OTC can be also decomposed to OTC 2 (m/z = 362.6) through demethylation, decarboxamidation, dihydroxylation, and deamidation reaction. The OTC 2 is transformed to OTC 5 (m/z = 318.3) by eliminating carbonyl, methyl, and hydroxyl groups. And the OTC 5 is fragmented, resulting in the forming of OTC 7 (m/z = 274) through the loss of amino groups and hydroxyl groups. Then the OTC 9 (m/z = 242) is formed. The third pathway can be described that through the loss of H_2O, OTC 3 (m/z = 426) is formed from OTC. Subsequently, some small molecular products including OTC 10 (m/z = 103.8), OTC 11 (m/z = 118), OTC 12 (m/z = 142), and OTC 13 (m/z = 130) are generated through oxidization of these intermediates (OTC 3, OTC 8, and OTC 9). Finally, these products are converted into H_2O and CO_2 which are the symbol of OTC mineralization during further oxidization reaction. The effect of TOC was performed at Fig. S7, and the result showed that the removal rate of TOC is about 75% within 30 min. These results above all demonstrated a good degradation capacity of Mn_xO_y@BC in removing OTC from aqueous environment.

3.3.3. Mechanism research

Results of the XPS diagram analysis of Mn in Mn_xO_y@BC indicated that the existence of Mn(II), Mn(III), and Mn(Ⅳ) in initial system and the characterizations of FTIR and Raman have also shown that there are C–O, C=O, O=C–O, and Mn–O bonds in the samples. In order to figure out the changes of manganese valence in materials, the analysis of XPS for Mn_xO_y@BC before and after reaction was studied. As reflected in Fig. S8, the content of Mn(III) showed slightly reduce while the content of Mn(Ⅳ) decreased from 22% to 15%, and the content of Mn(II) increased slightly. While from the change of solution color we can know

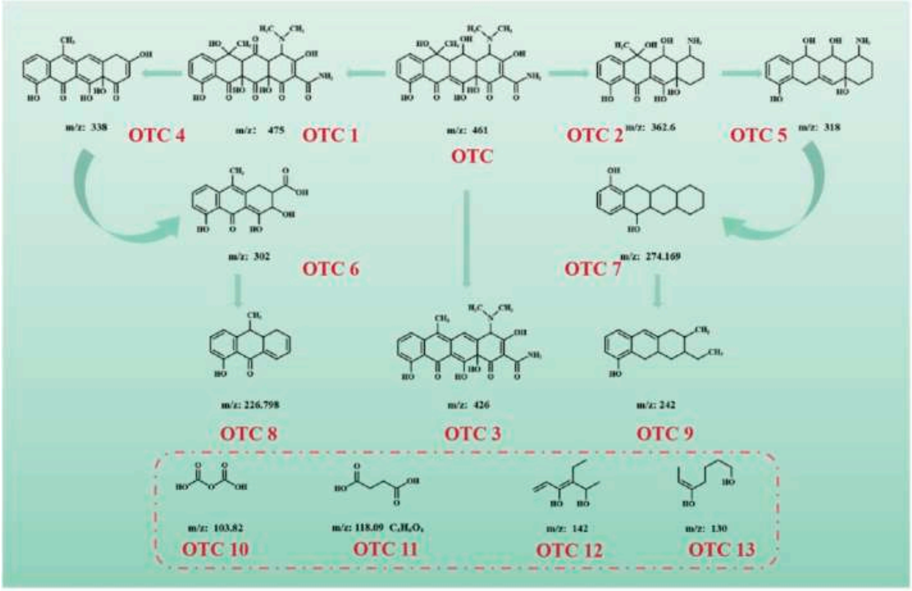

Fig. 5. The proposed degradation pathways of OTC.

that the conversion of Mn(II) and Mn(Ⅳ) is indeed existence. From these conclusions, the mechanism of this reaction is described as follows. In the whole reaction process, PI is activated and accompanied by manganese redox transformation. Fig. 6 illustrates the mechanism of this reaction. In the first part of the mechanism is the role of Mn active species in samples. Firstly, the Mn(Ⅳ) oxide, $^1O_2$, and $O_2^{\bullet-}$ can be produce by Mn(II) reacting with PI, where Mn(Ⅳ) existed in the form of Mn•O(OH)$_2$ along with the color of the solution changing from colorless to brown during the reaction (Eq. (1) – (2)) (Wang et al., 2012). Next, $^1O_2$ was further appeared by the interaction of $O_2^{\bullet-}$ with PI, for another way it can also be produced by the reduction of Mn(Ⅳ) (Eq. (3) – (4)). At the same time, was formed in water by the function of $O_2^{\bullet-}$ (Du et al., 2019). The second part of the mechanism belonged to the function of biochar. Biochar can also be an activator in the process of reaction from previous studies, and the oxygenated functional groups (OFGs) on biochar can donate electrons in mesoporous BC/PI system which are the key active sites for this reaction (Dai et al., 2021; He et al., 2021b). It can be seen from equation (5) – (6) that under the action between C−OH/-COOH and H_2O_2, •OH is produced. The third part must be the combined effects of Mn species and biochar, the Mn^{2+} (produced in Eq. (3)) is connected with BC-O•/BC-OO• (produced in Eq. (7)) and formed BC-O•–Mn^{2+}, which can also react with H_2O_2 and generate ROS in the system. In addition, some of the Mn in the samples aggregated to form clusters, indicating that some of the OTC couldn't contact with Mn active species directly. However, due to the adsorption of the biochar, the OTC can be adsorbed into the pores of biochar and thus react with Mn active species (Gopinath et al., 2021; Odinga et al., 2020). Besides, the transformation between Mn(III) and Mn(Ⅳ) was also involved in the whole reaction process which was triggered by electron transfer (Eq. (8) – (9)) (Zhang et al., 2021b). Finally, the OTC was degraded by ROS.

$$\mathrm{Mn(II)} + 2IO_4^- + O_2 + 3H_2O \rightarrow \mathrm{Mn{\bullet}O(OH)_2} + 2IO_3^- + 4H^+ + 2O_2^{\bullet-} \quad (1)$$

$$IO_4^- + 2O_2^{\bullet-} + H_2O \rightarrow IO_3^- + 2\,^1O_2 + 2OH^- \quad (2)$$

$$\mathrm{Mn{\bullet}O(OH)_2} + IO_4^- \rightarrow \mathrm{Mn{\bullet}(OH)_2} + IO_3^- + {}^1O_2 \quad (3)$$

$$2O_2^{\bullet-} + 2H_2O \rightarrow {}^1O_2 + H_2O_2 + 2OH^- \quad (4)$$

$$\mathrm{BC\text{-}OH} + H_2O_2 \rightarrow \mathrm{BC\text{-}O{\bullet}} + {\bullet}OH + H_2O \quad (5)$$

$$\mathrm{BC\text{-}COOH} + H_2O_2 \rightarrow \mathrm{BC\text{-}COO{\bullet}} + {\bullet}OH + H_2O \quad (6)$$

$$\mathrm{BC\text{-}O{\bullet}\text{–}Mn^{2+}} + H_2O_2 \rightarrow \mathrm{BC\text{-}O{\bullet}\text{—}Mn^{2+}} + {\bullet}OH \quad (7)$$

$$\mathrm{Mn(III)} + e^- \rightarrow \mathrm{Mn(II)} \quad (8)$$

$$2\mathrm{Mn(III)} + 2H_2O \rightarrow \mathrm{Mn(IV)} + \mathrm{Mn(II)} + 4H^+ \quad (9)$$

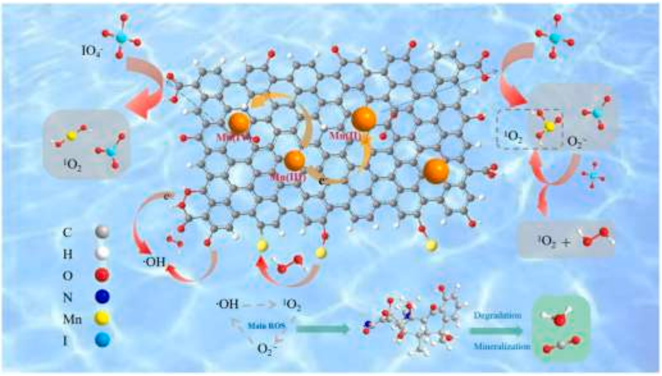

Fig. 6. Proposed mechanisms of PI activated by Mn_xO_y@BC for OTC degradation.

3.4. *Applications in different actual waters*

Three kinds of natural water samples were used in the experiment for investigating the applicability of Mn_xO_y@BC/PI system in nature environment. The waters were obtained from Peach water (Changsha, China), Xiangjiang water (Changsha, China), and tap water (Fig. S9). Table S4 has shown the characteristics of the water samples. Using deionized water as control sample, and for preventing the influence of bacteria in actual waters (Peach water and Xiangjiang water), sterilization experiment (T = 120 °C) was carried out before the reaction. Experimental results can be concluded that it is slightly inhibited in the two real water bodies compared with the degradation of OTC in deionized water, the reason could be proposed that sterilization results in the increase of organic matter content in water (Ratasuk et al., 2012). Although the removal was slightly inhibited, it still showed excellent efficiency (70%), and the degradation in tap water showed almost the same effect in control water. It can be deduced that Mn_xO_y@BC with excellent performance can be applied to actual waterbodies.

3.5. *Stability of Mn_xO_y@BC*

As shown in Fig. 7a, the leaching efficiency of manganese which were used in Mn_xO_y@BC/PI system under different pH conditions was investigated, the results showed that the leaching rates of Mn was higher in acidic conditions than alkaline, while in general, the leaching concentrations was relatively low. A good stability of Mn_xO_y@BC materials can be reflected with the XPS results. As shown in Fig. 7b, the change of surface element composition was not obvious through the whole process. The XPS spectra of Mn reflected that only part decreased in the reaction and changed slightly. And little manganese was lost in the whole process. Since the materials are put into use in actual production, its practicality must be considered. Therefore, four cycles were taken to investigate the stability of Mn_xO_y@BC (Fig. 7c). It is indicated that the system still had a high degradation rate to OTC after repeated use. Particularly, comparing with the first use, removal efficiency at the fourth reuse only decreased about 10%. Because the relevant raw materials for the preparation of Mn_xO_y@BC have wide sources range and low cost, they could be used as a promising and practical composites.

3.6. *Toxicity assessment of OTC and its degradation products*

In the process of OTC degradation, toxic intermediates may be produced. Therefore, it is necessary to evaluate the toxicity of these intermediates. In this study, the toxicity of OTC and its products were assessed by Toxicity Estimation Software Tool (T.E.S.T.), which based on the models of Quantitative Structure Activity Relationship (QSAR) (Dou et al., 2020). The assessment of toxicities were based on these levels: the lethal concentration of 50% (LC_{50}) (48h) daphnia magna, LD_{50} of oral rats, development toxicity, and mutagenicity. As seen in Fig. S10a-b, the acute toxicity of LC_{50}-48h and LD_{50} rats for OTC were 11.84 mg/L and 1140 mg/kg, respectively. The higher the value, the lower the toxicity (Jiang et al., 2020). It can be seen clearly that the main intermediates were all belonging to low-toxic substances. Notably, the increase value of the final products (OTC10, OTC11, OTC12, and OTC13) indicated the decrease of toxicity significantly. In addition, the development toxicity of OTC was 0.84, and the values of most degradation products were lower than that which was defined as "non-toxicant" (Fig. S10c) (Tang et al., 2020). From Fig. S10d, OTC can be classified as "mutagenicity positive" and most of the products were all defined as "mutagenicity negative". The results showed the low-toxic of the degradation products.

4. Conclusions

Nowadays, biochar is widely used as carbon-based activators in AOPs to remove organic pollution from water environment. In our work,

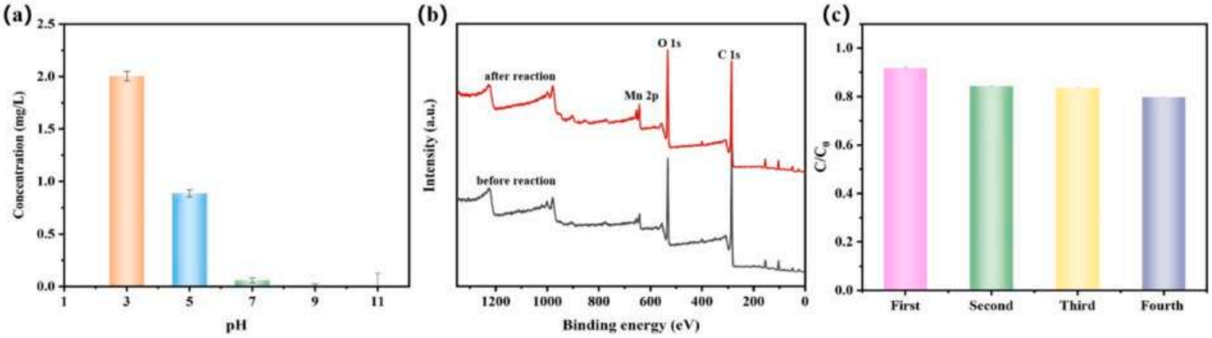

Fig. 7. The leaching efficiency of manganese in Mn_xO_y@BC under different pH conditions (a), XPS spectrum of Mn_xO_y@BC before and after reaction (b), and cycling runs for the photocatalytic degradation of OTC with Mn_xO_y@BC/PI system (c).

an excellent method by combing Mn_xO_y@BC with PI to remove OTC was proposed. The optimal experimental conditions were obtained with the PI concentration of 0.25 mM and the Mn_xO_y@BC dosage of 0.3 g/L. Various characteristic analysis proved that PI can be activated by Mn(II), Mn(III), and Mn(Ⅳ) to generate $O_2^{\bullet-}$ and $^1O_2$, respectively. Furthermore, $O_2^{\bullet-}$ can be converted to H_2O_2 with the activation of PI, and •OH can be formed under the reaction of H_2O_2 with biochar surface functional groups. Influencing factors including Mn_xO_y@BC and PI dosage, solution pH, HA, anions, and initial concentration of OTC were examined, and the results suggested wide adaptability of Mn_xO_y@BC in real wastewater. Based on the detected intermediates and characterization of major reactive species, three possible OTC degradation pathways were proposed. The high removal effect of different natural water and cycle-use analysis results also proved the sustainability of this composite. Moreover, it can stay a low leaching of Mn ions in the degradation process. Mn_xO_y@BC/PI system can provide a new direction for AOPs. However, in the process of our experiment, we have found that although it has low leaching amount, there was still a lot of space for improvement. And we also could try to prepare materials by hydrothermal method and apply them to solve different practical environmental problems.

Author statement

Guoge Fang: Conceptualization, Methodology, Software, Formal analysis, Investigation, Writing – original draft. **Jialing Li:** Conceptualization, Software, Writing – review & editing. **Chen Zhang:** Conceptualization, Resources, Supervision, Project administration, Funding acquisition. **Fanzhi Qin:** Conceptualization, Software, Writing – review & editing. **Hanzhuo Luo:** Methodology, Software, Writing – review & editing. **Cheng Huang**: Writing – review & editing. **Deyu Qin:** Writing – review & editing. **Zenglin Ouyang:** Writing – review & editing.

Declaration of competing interest

The authors declare that they have no known competing financial interests or personal relationships that could have appeared to influence the work reported in this paper.

Acknowledgements

This study was financially supported by the Program for the National Natural Science Foundation of China (52170162, 51809090), the Hunan Youth Talents Support Program (2021RC3049), the Natural Science Foundation of Hunan Province, China (2019JJ50077), and the Fundamental Research Funds for the Central Universities (531118010114).

Appendix A. Supplementary data

Supplementary data to this article can be found online at https://doi.org/10.1016/j.envpol.2022.118939.

References

Cao, M.H., Wang, B.B., Yu, H.S., Wang, L.L., Yuan, S.H., Chen, J., 2010. Photochemical decomposition of perfluorooctanoic acid in aqueous periodate with VUV and UV light irradiation. J. Hazard Mater. 179, 1143–1146. https://doi.org/10.1016/j.jhazmat.2010.02.030.

Chen, X., Oh, W.-D., Zhang, P.-H., Webster, R.D., Lim, T.-T., 2020. Surface construction of nitrogen-doped chitosan-derived carbon nanosheets with hierarchically porous structure for enhanced sulfacetamide degradation via peroxymonosulfate activation: maneuverable porosity and active sites. Chem. Eng. J. 382, 122908. https://doi.org/10.1016/j.cej.2019.122908.

Chia, L.-H., Tang, X., Weavers, L.K., 2004. Kinetics and mechanism of photoactivated periodate reaction with 4-chlorophenol in acidic solution. Environ. Sci. Technol. 38, 6875–6880. https://doi.org/10.1021/es049155n.

Cuong, D.V., Wu, P.-C., Chen, L.-I., Hou, C.-H., 2021. Active MnO_2/biochar composite for efficient As(III) removal: insight into the mechanisms of redox transformation and adsorption. Water Res. 188, 116495. https://doi.org/10.1016/j.watres.2020.116495.

Dai, L., Lu, Q., Zhou, H., Shen, F., Liu, Z., Zhu, W., Huang, H., 2021. Tuning oxygenated functional groups on biochar for water pollution control: a critical review. J. Hazard Mater. 420, 126547. https://doi.org/10.1016/j.jhazmat.2021.126547.

Dou, M., Wang, J., Gao, B., Xu, C., Yang, F., 2020. Photocatalytic difference of amoxicillin and cefotaxime under visible light by mesoporous g-C_3N_4: mechanism, degradation pathway and DFT calculation. Chem. Eng. J. 383, 123134. https://doi.org/10.1016/j.cej.2019.123134.

Du, J., Tang, S., Faheem, Ling, H., Zheng, H., Xiao, G., Luo, L., Bao, J., 2019. Insights into periodate oxidation of bisphenol A mediated by manganese. Chem. Eng. J. 369, 1034–1039. https://doi.org/10.1016/j.cej.2019.03.158.

Du, J., Xiao, G., Xi, Y., Zhu, X., Su, F., Kim, S.H., 2020. Periodate activation with manganese oxides for sulfanilamide degradation. Water Res. 169, 115278. https://doi.org/10.1016/j.watres.2019.115278.

Fang, G., Liu, C., Wang, Y., Dionysiou, D.D., Zhou, D., 2017. Photogeneration of reactive oxygen species from biochar suspension for diethyl phthalate degradation. Appl. Catal., B 214, 34–45. https://doi.org/10.1016/j.apcatb.2017.05.036.

Feng, L., Yuan, G., Xiao, L., Wei, J., Bi, D., 2021. Biochar modified by nano-manganese dioxide as adsorbent and oxidant for oxytetracycline. Bull. Environ. Contam. Toxicol. 107, 269–275. https://doi.org/10.1007/s00128-020-02813-0.

Gopinath, K.P., Vo, D.-V.N., Gnana Prakash, D., Adithya Joseph, A., Viswanathan, S., Arun, J., 2021. Environmental applications of carbon-based materials: a review. Environ. Chem. Lett. 19, 557–582. https://doi.org/10.1007/s10311-020-01084-9.

Guo, H., Niu, H.-Y., Liang, C., Niu, C.-G., Huang, D.-W., Zhang, L., Tang, N., Yang, Y., Feng, C.-Y., Zeng, G.-M., 2019. Insight into the energy band alignment of magnetically separable $Ag_2O/ZnFe_2O_4$ p-n heterostructure with rapid charge transfer assisted visible light photocatalysis. J. Catal. 370, 289–303. https://doi.org/10.1016/j.jcat.2019.01.009.

Guo, Y., Yan, L., Li, X., Yan, T., Song, W., Hou, T., Tong, C., Mu, J., Xu, M., 2021. Goethite/biochar-activated peroxymonosulfate enhances tetracycline degradation: inherent roles of radical and non-radical processes. Sci. Total Environ. 783, 147102. https://doi.org/10.1016/j.scitotenv.2021.147102.

He, L., Lv, L., Pillai, S.C., Wang, H., Xue, J., Ma, Y., Liu, Y., Chen, Y., Wu, L., Zhang, Z., Yang, L., 2021a. Efficient degradation of diclofenac sodium by periodate activation using Fe/Cu bimetallic modified sewage sludge biochar/UV system. Sci. Total Environ. 783, 146974. https://doi.org/10.1016/j.scitotenv.2021.146974.

He, X., Zheng, N., Hu, R., Hu, Z., Yu, J.C., 2021b. Hydrothermal and pyrolytic conversion of biomasses into catalysts for advanced oxidation treatments. Adv. Funct. Mater. 31, 2006505. https://doi.org/10.1002/adfm.202006505.

He, Y., Tian, Z., Yi, Q., Zhang, Y., Yang, M., 2020. Impact of oxytetracycline on anaerobic wastewater treatment and mitigation using enhanced hydrolysis pretreatment. Water Res. 187, 116408. https://doi.org/10.1016/j.watres.2020.116408.

Huang, D., Hu, C., Zeng, G., Cheng, M., Xu, P., Gong, X., Wang, R., Xue, W., 2017a. Combination of Fenton processes and biotreatment for wastewater treatment and soil remediation. Sci. Total Environ. 574, 1599–1610. https://doi.org/10.1016/j.scitotenv.2016.08.199.

Huang, D., Wang, X., Zhang, C., Zeng, G., Peng, Z., Zhou, J., Cheng, M., Wang, R., Hu, Z., Qin, X., 2017b. Sorptive removal of ionizable antibiotic sulfamethazine from aqueous solution by graphene oxide-coated biochar nanocomposites: influencing factors and mechanism. Chemosphere 186, 414–421. https://doi.org/10.1016/j.chemosphere.2017.07.154.

Ishii, M., Nakahira, M., Yamanaka, T., 1972. Infrared absorption spectra and cation distributions in (Mn, Fe)$_3O_4$. Solid State Commun. 11, 209–212. https://doi.org/10.1016/0038-1098(72)91162-3.

Jia, X., Zhou, J., Liu, J., Liu, P., Yu, L., Wen, B., Feng, Y., 2020. The antimony sorption and transport mechanisms in removal experiment by Mn-coated biochar. Sci. Total Environ. 724, 138158. https://doi.org/10.1016/j.scitotenv.2020.138158.

Jiang, J., Wang, X., Liu, Y., Ma, Y., Li, T., Lin, Y., Xie, T., Dong, S., 2020. Photo-Fenton degradation of emerging pollutants over Fe-POM nanoparticle/porous and ultrathin g-C_3N_4 nanosheet with rich nitrogen defect: degradation mechanism, pathways, and products toxicity assessment. Appl. Catal., B 278, 119349. https://doi.org/10.1016/j.apcatb.2020.119349.

Jin, X., Xu, H., Qiu, S., Jia, M., Wang, F., Zhang, A., Jiang, X., 2017. Direct photolysis of oxytetracycline: influence of initial concentration, pH and temperature. J. Photochem. Photobiol. Chem. 332, 224–231. https://doi.org/10.1016/j.jphotochem.2016.08.032.

Kumar, M., Xiong, X., Sun, Y., Yu, I.K.M., Tsang, D.C.W., Hou, D., Gupta, J., Bhaskar, T., Pandey, A., 2020. Critical review on biochar-supported catalysts for pollutant degradation and sustainable biorefinery. Adv. Sustainable Syst. 4, 1900149. https://doi.org/10.1002/adsu.201900149.

Lee, Y.-C., Chen, M.-J., Huang, C.-P., Kuo, J., Lo, S.-L., 2016. Efficient sonochemical degradation of perfluorooctanoic acid using periodate. Ultrason. Sonochem. 31, 499–505. https://doi.org/10.1016/j.ultsonch.2016.01.030.

Li, Z., Sun, Y., Yang, Y., Han, Y., Wang, T., Chen, J., Tsang, D.C.W., 2020. Biochar-supported nanoscale zero-valent iron as an efficient catalyst for organic degradation in groundwater. J. Hazard Mater. 383, 121240. https://doi.org/10.1016/j.jhazmat.2019.121240.

Lin, H., Qiu, S., Wu, Z., Ye, X., Liu, M., 2021. Fabrication of lignin-based biochar containing multi-metal ferrite and efficient removal for oxytetracycline hydrochloride. J. Clean. Prod., 129885 https://doi.org/10.1016/j.jclepro.2021.129885.

Liu, S., Lai, C., Li, B., Zhang, C., Zhang, M., Huang, D., Qin, L., Yi, H., Liu, X., Huang, F., Zhou, X., Chen, L., 2020. Role of radical and non-radical pathway in activating persulfate for degradation of p-nitrophenol by sulfur-doped ordered mesoporous carbon. Chem. Eng. J. 384, 123304. https://doi.org/10.1016/j.cej.2019.123304.

Luo, H., Lin, Q., Zhang, X., Huang, Z., Liu, S., Jiang, J., Xiao, R., Liao, X., 2019. New insights into the formation and transformation of active species in nZVI/BC activated persulfate in alkaline solutions. Chem. Eng. J. 359, 1215–1223. https://doi.org/10.1016/j.cej.2018.11.056.

Luo, J., Li, X., Ge, C., Müller, K., Yu, H., Deng, H., Shaheen, S.M., Tsang, D.C.W., Bolan, N.S., Rinklebe, J., Ok, Y.S., Gao, B., Wang, H., 2021. Preparation of ammonium-modified cassava waste-derived biochar and its evaluation for synergistic adsorption of ternary antibiotics from aqueous solution. J. Environ. Manag. 298, 113530. https://doi.org/10.1016/j.jenvman.2021.113530.

Ma, J., Graham, N.J.D., 2000. Degradation of atrazine by manganese-catalysed ozonation—influence of radical scavengers. Water Res. 34, 3822–3828. https://doi.org/10.1016/S0043-1354(00)00130-5.

Melia, P.M., Busquets, R., Hooda, P.S., Cundy, A.B., Sohi, S.P., 2019. Driving forces and barriers in the removal of phosphorus from water using crop residue, wood and sewage sludge derived biochars. Sci. Total Environ. 675, 623–631. https://doi.org/10.1016/j.scitotenv.2019.04.232.

Meng, L., Yin, W., Wang, S., Wu, X., Hou, J., Yin, W., Feng, K., Ok, Y.S., Wang, X., 2020. Photocatalytic behavior of biochar-modified carbon nitride with enriched visible-light reactivity. Chemosphere 239, 124713. https://doi.org/10.1016/j.chemosphere.2019.124713.

Odinga, E.S., Waigi, M.G., Gudda, F.O., Wang, J., Yang, B., Hu, X., Li, S., Gao, Y., 2020. Occurrence, formation, environmental fate and risks of environmentally persistent free radicals in biochars. Environ. Int. 134, 105172. https://doi.org/10.1016/j.envint.2019.105172.

Pei, X.-Y., Ren, H.-Y., Liu, G.-S., Cao, G.-L., Xie, G.-J., Xing, D.-F., Ren, N.-Q., Liu, B.-F., 2022. Non-radical mechanism and toxicity analysis of β-cyclodextrin functionalized biochar catalyzing the degradation of bisphenol A and its analogs by peroxydisulfate. J. Hazard Mater. 424, 127254. https://doi.org/10.1016/j.jhazmat.2021.127254.

Peng, H., Gao, P., Chu, G., Pan, B., Peng, J., Xing, B., 2017. Enhanced adsorption of Cu(II) and Cd(II) by phosphoric acid-modified biochars. Environ. Pollut. 229, 846–853. https://doi.org/10.1016/j.envpol.2017.07.004.

Qin, F., Li, J., Zhang, C., Zeng, G., Huang, D., Tan, X., Qin, D., Tan, H., 2021. Biochar in the 21st century: a data-driven visualization of collaboration, frontier identification, and future trend. Sci. Total Environ., 151774 https://doi.org/10.1016/j.scitotenv.2021.151774.

Qin, F., Peng, Y., Song, G., Fang, Q., Wang, R., Zhang, C., Zeng, G., Huang, D., Lai, C., Zhou, Y., Tan, X., Cheng, M., Liu, S., 2020. Degradation of sulfamethazine by biochar-supported bimetallic oxide/persulfate system in natural water: performance and reaction mechanism. J. Hazard Mater. 398, 122816. https://doi.org/10.1016/j.jhazmat.2020.122816.

Ratasuk, N., Boonsaner, M., Hawker, D.W., 2012. Effect of temperature, pH and illumination on abiotic degradation of oxytetracycline in sterilized swine manure. J. Environ. Sci. Health, Part A 47, 1687–1694. https://doi.org/10.1080/10934529.2012.687274.

Shen, Z., Zhang, J., Hou, D., Tsang, D.C.W., Ok, Y.S., Alessi, D.S., 2019. Synthesis of MgO-coated corncob biochar and its application in lead stabilization in a soil washing residue. Environ. Int. 122, 357–362. https://doi.org/10.1016/j.envint.2018.11.045.

Song, G., Qin, F., Yu, J., Tang, L., Pang, Y., Zhang, C., Wang, J., Deng, L., 2022. Tailoring biochar for persulfate-based environmental catalysis: impact of biomass feedstocks. J. Hazard Mater. 424, 127663. https://doi.org/10.1016/j.jhazmat.2021.127663.

Song, H., Li, Q., Ye, Y., Pan, F., Zhang, D., Xia, D., 2021. Degradation of cephalexin by persulfate activated with magnetic loofah biochar: performance and mechanism. Separ. Purif. Technol. 272, 118971. https://doi.org/10.1016/j.seppur.2021.118971.

Stephan, A.M., Kumar, T.P., Ramesh, R., Thomas, S., Jeong, S.K., Nahm, K.S., 2006. Pyrolitic carbon from biomass precursors as anode materials for lithium batteries. Mater. Sci. Eng. 430, 132–137. https://doi.org/10.1016/j.msea.2006.05.131.

Sun, H., He, F., Choi, W., 2020. Production of reactive oxygen species by the reaction of periodate and hydroxylamine for rapid removal of organic pollutants and waterborne bacteria. Environ. Sci. Technol. 54, 6427–6437. https://doi.org/10.1021/acs.est.0c00817.

Tan, H., Li, J., He, M., Li, J., Zhi, D., Qin, F., Zhang, C., 2021. Global evolution of research on green energy and environmental technologies:A bibliometric study. J. Environ. Manag. 297, 113382. https://doi.org/10.1016/j.jenvman.2021.113382.

Tan, X., Wei, W., Xu, C., Meng, Y., Bai, W., Yang, W., Lin, A., 2020. Manganese-modified biochar for highly efficient sorption of cadmium. Environ. Sci. Pollut. Res. 27, 9126–9134. https://doi.org/10.1007/s11356-019-07059-w.

Tang, S., Wang, Z., Yuan, D., Zhang, C., Rao, Y., Wang, Z., Yin, K., 2020. Ferrous ion-tartaric acid chelation promoted calcium peroxide fenton-like reactions for simulated organic wastewater treatment. J. Clean. Prod. 268, 122253. https://doi.org/10.1016/j.jclepro.2020.122253.

Trakal, L., Veselská, V., Šafařík, I., Vítková, M., Číhalová, S., Komárek, M., 2016. Lead and cadmium sorption mechanisms on magnetically modified biochars. Bioresour. Technol. 203, 318–324. https://doi.org/10.1016/j.biortech.2015.12.056.

Wan, C., Jiao, Y., Li, J., 2016. Core–shell composite of wood-derived biochar supported MnO_2 nanosheets for supercapacitor applications. RSC Adv. 6, 64811–64817. https://doi.org/10.1039/C6RA12043A.

Wang, M., Tan, W., Feng, X., Koopal, L.K., Liu, M., Liu, F., 2012. One-step synthesis of sea urchin-like α-MnO_2 using KIO_4 as the oxidant and its oxidation of arsenite. Mater. Lett. 77, 60–62. https://doi.org/10.1016/j.matlet.2012.03.005.

Wang, R.-Z., Huang, D.-L., Liu, Y.-G., Zhang, C., Lai, C., Zeng, G.-M., Cheng, M., Gong, X.-M., Wan, J., Luo, H., 2018. Investigating the adsorption behavior and the relative distribution of Cd^{2+} sorption mechanisms on biochars by different feedstock. Bioresour. Technol. 261, 265–271. https://doi.org/10.1016/j.biortech.2018.04.032.

Wang, Z., Xu, X., Ma, S., Wang, H., Zhao, H., Wang, Y., Tong, S., Su, Z., Wang, W., Bai, J., 2021. The superior adsorption capacity of boron-nitrogen co-doping walnut shell biochar powder for Au(III), Pt(IV), and Pd(II). J. Environ. Chem. Eng. 9, 106288. https://doi.org/10.1016/j.jece.2021.106288.

Xiang, Y., Yang, X., Xu, Z., Hu, W., Zhou, Y., Wan, Z., Yang, Y., Wei, Y., Yang, J., Tsang, D.C.W., 2020. Fabrication of sustainable manganese ferrite modified biochar from vinasse for enhanced adsorption of fluoroquinolone antibiotics: effects and mechanisms. Sci. Total Environ. 709, 136079. https://doi.org/10.1016/j.scitotenv.2019.136079.

Xu, C., Wen, D., Zhu, Q., Zhu, H., Zhang, Y., Huang, D., 2017. Effects of peanut shell biochar on the adsorption of Cd(II) by paddy soil. Bull. Environ. Contam. Toxicol. 98, 413–419. https://doi.org/10.1007/s00128-016-1973-6.

Xu, R., Li, M., Zhang, Q., 2022. Collaborative optimization for the performance of ZnO/biochar composites on persulfate activation through plant enrichment-pyrolysis method. Chem. Eng. J. 429, 132294. https://doi.org/10.1016/j.cej.2021.132294.

Xu, X., Chen, J., Wang, S., Ge, J., Qu, R., Feng, M., Sharma, V.K., Wang, Z., 2018. Degradation kinetics and transformation products of chlorophene by aqueous permanganate. Water Res. 138, 293–300. https://doi.org/10.1016/j.watres.2018.03.057.

Yan, S., Zhang, X., Shi, Y., Zhang, H., 2018. Natural Fe-bearing manganese ore facilitating bioelectro-activation of peroxymonosulfate for bisphenol A oxidation. Chem. Eng. J. 354, 1120–1131. https://doi.org/10.1016/j.cej.2018.08.066.

Yang, X., Wu, P., Chu, W., Wei, G., 2021a. Peroxymonosulfate/$LaCoO_3$ system for tetracycline degradation: performance and effects of co-existing inorganic anions and natural organic matter. J. Water Proc. Eng. 43, 102231. https://doi.org/10.1016/j.jwpe.2021.102231.

Yang, Y., Li, X., Zhou, C., Xiong, W., Zeng, G., Huang, D., Zhang, C., Wang, W., Song, B., Tang, X., Li, X., Guo, H., 2020a. Recent advances in application of graphitic carbon nitride-based catalysts for degrading organic contaminants in water through advanced oxidation processes beyond photocatalysis: a critical review. Water Res. 184, 116200. https://doi.org/10.1016/j.watres.2020.116200.

Yang, Y., Zeng, G., Huang, D., Zhang, C., He, D., Zhou, C., Wang, W., Xiong, W., Li, X., Li, B., Dong, W., Zhou, Y., 2020b. Molecular engineering of polymeric carbon nitride for highly efficient photocatalytic oxytetracycline degradation and H_2O_2 production. Appl. Catal., B 272, 118970. https://doi.org/10.1016/j.apcatb.2020.118970.

Yang, Y., Zhang, C., Huang, D., Zeng, G., Huang, J., Lai, C., Zhou, C., Wang, W., Guo, H., Xue, W., Deng, R., Cheng, M., Xiong, W., 2019. Boron nitride quantum dots decorated ultrathin porous g-C_3N_4: intensified exciton dissociation and charge transfer for promoting visible-light-driven molecular oxygen activation. Appl. Catal., B 245, 87–99. https://doi.org/10.1016/j.apcatb.2018.12.049.

Yang, Z., Wang, Z., Liang, G., Zhang, X., Xie, X., 2021b. Catalyst bridging-mediated electron transfer for nonradical degradation of bisphenol A via natural manganese ore-cornstalk biochar composite activated peroxymonosulfate. Chem. Eng. J. 426, 131777. https://doi.org/10.1016/j.cej.2021.131777.

Ye, S., Yan, M., Tan, X., Liang, J., Zeng, G., Wu, H., Song, B., Zhou, C., Yang, Y., Wang, H., 2019. Facile assembled biochar-based nanocomposite with improved graphitization for efficient photocatalytic activity driven by visible light. Appl. Catal., B 250, 78–88. https://doi.org/10.1016/j.apcatb.2019.03.004.

Yun, E.-T., Yoo, H.-Y., Kim, W., Kim, H.-E., Kang, G., Lee, H., Lee, S., Park, T., Lee, C., Kim, J.-H., Lee, J., 2017. Visible-light-induced activation of periodate that mimics dye-sensitization of TiO_2: simultaneous decolorization of dyes and production of oxidizing radicals. Appl. Catal., B 203, 475–484. https://doi.org/10.1016/j.apcatb.2016.10.029.

Zhang, C., He, D., Fu, S., Zeng, G., Liang, Q., Yang, Y., Huang, D., Wang, W., Zhou, Y., 2021a. Silver iodide decorated $ZnSn(OH)_6$ hollow cube: room-temperature preparation and application for highly efficient photocatalytic oxytetracycline degradation. Chem. Eng. J. 421, 129810. https://doi.org/10.1016/j.cej.2021.129810.

Zhang, C., Lai, C., Zeng, G., Huang, D., Yang, C., Wang, Y., Zhou, Y., Cheng, M., 2016. Efficacy of carbonaceous nanocomposites for sorbing ionizable antibiotic sulfamethazine from aqueous solution. Water Res. 95, 103–112. https://doi.org/10.1016/j.watres.2016.03.014.

Zhang, C., Qin, D., Zhou, Y., Qin, F., Wang, H., Wang, W., Yang, Y., Zeng, G., 2022. Dual optimization approach to Mo single atom dispersed g-C_3N_4 photocatalyst: morphology and defect evolution. Appl. Catal., B 303, 120904. https://doi.org/10.1016/j.apcatb.2021.120904.

Zhang, C., Tian, S., Qin, F., Yu, Y., Huang, D., Duan, A., Zhou, C., Yang, Y., Wang, W., Zhou, Y., Luo, H., 2021b. Catalyst-free activation of permanganate under visible light irradiation for sulfamethazine degradation: experiments and theoretical calculation. Water Res. 194, 116915. https://doi.org/10.1016/j.watres.2021.116915.

Zhang, C., Wang, W., Duan, A., Zeng, G., Huang, D., Lai, C., Tan, X., Cheng, M., Wang, R., Zhou, C., Xiong, W., Yang, Y., 2019a. Adsorption behavior of engineered carbons and carbon nanomaterials for metal endocrine disruptors: experiments and theoretical calculation. Chemosphere 222, 184–194. https://doi.org/10.1016/j.chemosphere.2019.01.128.

Zhang, C., Zeng, G., Huang, D., Lai, C., Chen, M., Cheng, M., Tang, W., Tang, L., Dong, H., Huang, B., Tan, X., Wang, R., 2019b. Biochar for environmental management: mitigating greenhouse gas emissions, contaminant treatment, and potential negative impacts. Chem. Eng. J. 373, 902–922. https://doi.org/10.1016/j.cej.2019.05.139.

Zhang, S., Zhao, S., Huang, S., Hu, B., Wang, M., Zhang, Z., He, L., Du, M., 2021c. Photocatalytic degradation of oxytetracycline under visible light by nanohybrids of CoFe alloy nanoparticles and nitrogen-/sulfur-codoped mesoporous carbon. Chem. Eng. J. 420, 130516. https://doi.org/10.1016/j.cej.2021.130516.

Zhao, N., Liu, K., He, C., Gao, J., Zhang, W., Zhao, T., Tsang, D.C.W., Qiu, R., 2020. Singlet oxygen mediated the selective removal of oxytetracycline in C/Fe_3C/Fe^0 system as compared to chloramphenicol. Environ. Int. 143, 105899. https://doi.org/10.1016/j.envint.2020.105899.

Zhong, Q., Lin, Q., He, W., Fu, H., Huang, Z., Wang, Y., Wu, L., 2021. Study on the nonradical pathways of nitrogen-doped biochar activating persulfate for tetracycline degradation. Separ. Purif. Technol. 276, 119354. https://doi.org/10.1016/j.seppur.2021.119354.

Zhou, J., Song, H., Ma, L., Chen, X., 2011. Magnetite/graphene nanosheet composites: interfacial interaction and its impact on the durable high-rate performance in lithium-ion batteries. RSC Adv. 1, 782–791. https://doi.org/10.1039/C1RA00402F.

Zhou, X., Lai, C., Liu, S., Li, B., Qin, L., Liu, X., Yi, H., Fu, Y., Li, L., Zhang, M., Yan, H., Wang, J., Chen, M., Zeng, G., 2021. Activation of persulfate by swine bone derived biochar: insight into the specific role of different active sites and the toxicity of acetaminophen degradation pathways. Sci. Total Environ. 151059 https://doi.org/10.1016/j.scitotenv.2021.151059.

Zhou, Y., Zhang, C., Huang, D., Wang, W., Zhai, Y., Liang, Q., Yang, Y., Tian, S., Luo, H., Qin, D., 2022. Structure defined 2D Mo_2C/2Dg-C_3N_4 Van der Waals heterojunction: oriented charge flow in-plane and separation within the interface to collectively promote photocatalytic degradation of pharmaceutical and personal care products. Appl. Catal., B 301, 120749. https://doi.org/10.1016/j.apcatb.2021.120749.

Zong, Y., Shao, Y., Zeng, Y., Shao, B., Xu, L., Zhao, Z., Liu, W., Wu, D., 2021. Enhanced oxidation of organic contaminants by iron(II)-Activated periodate: the significance of high-valent iron–oxo species. Environ. Sci. Technol. 55, 7634–7642. https://doi.org/10.1021/acs.est.1c00375.